Cytosolic Proteostatic Adaptation to Mitochondrial Stress Causes Progressive Muscle Wasting

Xiaowen Wang [1], Frank A. Middleton[2], Rabi Tawil[3] & Xin Jie Chen[1, 2] *

[1]Department of Biochemistry and Molecular Biology, and [2]Neuroscience and Physiology, State University of New York Upstate Medical University, Syracuse, NY 13210, USA. [3]Department of Neurology, University of Rochester, Rochester, NY 14642, USA.

*Corresponding author: Department of Biochemistry and Molecular Biology, State University of New York Upstate Medical University, 750 East Adams Street, Syracuse, NY 13210, USA. Tel: (315) 464-8723; Fax: (315) 464-8750; Email: chenx@upstate.edu

ABSTRACT

Muscle wasting (or atrophy), defined by reduced myofiber size and muscle strength, occurs in primary neuromuscular diseases and during aging. The progressive loss of muscle mass with aging is known as sarcopenia, and affects 35.4% and 75.5% of women and men over 60 years of age, respectively [1]. Mitochondrial dysfunction has been proposed to contribute to progressive muscle wasting [2, 3]. Interestingly, substantial levels of bioenergetic deficiency and oxidative stress seem to be insufficient by themselves to intrinsically cause muscle wasting during aging[4]. This raises the possibility that mitochondria may affect muscle mass by additional mechanisms. Here, we show that chronic adaptations to mitochondrial protein overload cause muscle wasting. Protein overloading, together with conditions that directly and indirectly affect the protein import machinery, are known triggers of mitochondrial Precursor Over-accumulation Stress (mPOS), a newly discovered cellular stress mechanism caused by toxic accumulation of precursor proteins in the cytosol [5-7]. Our evidence was obtained from transgenic mice that were generated to have a two-fold increase in the nuclear-encoded Ant1 protein that is involved in ATP/ADP exchange on the inner mitochondrial membrane (IMM). These animals progressively lost muscle mass with age, although their lifespan was unaffected. At two years of age, the skeletal muscle of these mice was severely atrophic. The *ANT1*-transgenic muscles have a drastically remodeled transcriptome that appears trying to counteract mPOS, by repressing protein synthesis and stimulating proteasomal function, autophagy, lysosomal amplification and Gadd45a-signaling. These processes are all known to promote muscle wasting [8, 9]. Thus, chronic proteostatic adaptation to mPOS is a robust mechanism of muscle wasting. These findings may help improve the understanding of how mitochondria contribute to muscle wasting during aging.

They may also have direct implications for human diseases associated with *ANT1* overexpression [10-12].

RESULTS AND DISCUSSION

Our recent studies showed that overloading of mitochondria with carrier proteins leads to the accumulation of unimported mitochondrial proteins in the cytosol, followed by proteostatic stress (or mPOS) and cell death [5]. However, it is unknown whether mPOS can occur *in vivo* and whether it causes pathology. To address this, we prepared transgenic mice overexpressing *ANT1*, encoding an adenine nucleotide carrier on the IMM. An earlier study reported the use of transgenic mice expressing *ANT1* cDNA from the human α-skeletal actin promoter to model Facioscapulohumeral Dystrophy (FSHD)[13]. These mice did not develop muscle pathology. However, that study failed to examine whether or not the Ant1 protein was actually overexpressed compared to control animals, which was a considerable limitation given that Ant1 is highly abundant in muscle mitochondria[14]. Thus, whether *ANT1* overexpression does, or does not, cause muscle pathology remains undetermined. To address this, we generated *ANT1*-transgenic mice using the *ANT1* genomic locus and its native promoter (Fig. 1a). The resulting hemizygous transgenic mice (hereafter referred to as $ANT1^{Tg}/+$) are kyphotic, and have reduced body weight, with more pronounced effects in males than in females (Extended Data Fig. 1a-1d). We mainly focused our studies on a specific transgenic line, in which Ant1 levels are increased by only two-fold in the skeletal muscles (Fig. 1b and 1c).

The $ANT1^{Tg}/+$ mice have a normal body length (Fig. 1d). They have increased spinal curvature (Fig. 1e), decreased home cage activity, and reduced exercise tolerance (Extended Data Fig. 1f-1m), which suggests muscle weakness. Gait abnormalities become noticeable from the age

of 6 months and progressively deteriorate during aging (Fig. 1f; Supplemental video 1-3). Parallel to reduced body weight (Fig. 1g), the female and male mice lose lean mass by 24.18% and 26.64% respectively at 6 months, and by 35.01% and 36.28% respectively at 12 months of age (Fig. 1h). Skeletal muscle becomes severely atrophic at two years of age (Fig. 1i), while the overall lifespan is unaffected (Extended Data Fig. 1e). Supporting muscle wasting, the *ANT1*^{Tg}/+ mice have increased myofiber size variability (Fig. 1j), with an overall reduction in average myofiber diameter of 26.18% and 49.46% at 12 and 20 months of age, respectively (Fig. 1k; Extended Data Fig. 2a and 2b). Round- and angular-shaped myofibers, and mild increase of endomysial connective tissues were observed in the *ANT1*-transgenic muscles (Fig. 1l and Extended Data Fig. 2c-2f). No myofiber type grouping suggestive of a chronic neuropathic process was observed. Furthermore, the *ANT1*^{Tg}/+ muscles have increased basophilic stippling, suggesting increased acidic cellular components (Extended Data Fig. 3a). Moth-eaten myofibers were detected in the *ANT1*^{Tg}/+ muscles, as indicated by poor staining of NADH, succinate dehydrogenase (SDH) and cytochrome *c* oxidase (COX) (Fig. 2a). The level of the proapoptotic Bax protein is elevated but without an increase in the percentage of central nuclei (Extended Data Fig. 3b-3d). Taken together, we conclude that *ANT1*-overexpression likely causes progressive muscle wasting mainly because of processes that lead to reduced myofiber size.

We found that Ant1 overexpression has a moderate effect on mitochondrial function. The assembly of respiratory complexes and supercomplexes is not noticeably affected (Fig. 2b and 2c). The state-3 and state-4 respiratory rates are only moderately reduced (Fig. 2d). The overall respiratory control ratio is unaffected, suggesting that moderate *ANT1*-overexpression is insufficient to uncouple mitochondrial respiration (Fig. 2e). Previous studies showed that more

severe bioenergetic deficiencies are not sufficient to induce muscle wasting during aging, raising the possibility that additional factors likely cause *ANT1*-induced muscle pathology.

To understand how *ANT1* induces muscle wasting, we analyzed the transcriptome of *ANT1*^{Tg}/+ skeletal muscles. We identified 4,947 genes expressed at reliable levels (Fig. 3a), among which 1,016 genes were differentially expressed in the *ANT1*^{Tg}/+ versus wild-type (WT) muscles (two-way ANOVA, $q < 0.05$; Supplemental Table 1). Among these genes, 285 genes were upregulated and 78 genes down-regulated at the ±1.5 fold level, and 38 genes were up-regulated and 6 down-regulated at the ±5 fold level (Fig. 3b). Interestingly, out of the top 20 genes previously identified as upregulated in sarcopenia[15], we found 6 are activated in the *ANT1*^{Tg}/+ muscles (Fig. 3c; Supplemental Table 2), suggesting that the *ANT1*-overexpressing and aging muscles share at least some overlapping stresses. Consistent with our evidence of a mild bioenergetic defect, genes involved in oxidative phosphorylation and anti-oxidant defense were not over-represented among the significantly upregulated genes. Instead, genes for Integrated Stress Response (ISR, Fig. 3d), One-Carbon Metabolism and the Starvation Response are upregulated (Supplemental Table 3). These transcriptional signatures have previously been reported in mitochondrial disease models[16-18]. Phosphorylation of eIF2α, the central player in the ISR, was increased in *ANT1*^{Tg}/+ muscles (Fig. 3e). This eIF2α phosphorylation is likely responsible for the upregulation of *ATF4*, *ATF5*, *DDIT3* and *NUPR1* (Fig. 3d), by promoting cap-independent translation of these transcriptional factors followed by a feed-forward loop of transcriptional activation[19]. We found that eIF2α phosphorylation is elevated in aged muscles not only in *ANT1*^{Tg}/+ but also wild-type mice (Extended Data Fig. 4). Phosphorylated eIF2α globally attenuates cap-dependent translation in response to various stresses including mitochondrial damage[20]. Thus, our data support a global proteostatic stress state in *ANT1*^{Tg}/+ muscles, and

perhaps also in the physiologically aged muscles. Additionally, we observed the upregulation of genes for protein import and mitochondrial chaperones (Fig. 3g). This is reminiscent of the mitochondrial Compromised Protein import Response (mitoCPR) and the mitochondrial Unfolded Protein Response (mtUPR) mechanisms, which are important for improving protein import and mitochondrial homeostasis [21, 22]. These data show that *ANT1*-overexpression induces both protein import and proteostatic stresses in mitochondria, and proteostatic stress in the cytosol (mPOS).

More importantly, RNA-Seq also revealed other proteostatic responses in *ANT1*^{Tg}/+ muscles in addition to eIF2α phosphorylation, with some of them being downstream targets of the ISR. First, expression of several cytosolic chaperones and the heat shock transcriptional factor 1 (HSF1) are increased (Extended Data Fig. 5a). Secondly, we found that the phosphorylation of Rps6 kinase (S6K) is not decreased in *ANT1*^{Tg}/+ muscles, suggesting that mTOR-signaling is not attenuated (Extended Data Fig. 5b & 5c). Interestingly, the transcription of *EIF4EBP1* (or *4EBP1*), a downstream target of the ISR[23], is increased (Fig. 4a). Consequently, both 4EBP1 and its phosphorylated form, P-4EBP1, are increased (Fig. 4b-4d). The non-phosphorylated 4EBP is a repressor of protein translation. Thirdly, we found that the overall levels of ubiquitinated proteins, and p62 that promotes the formation and removal of ubiquitinated and aggregated proteins, are not increased in the *ANT1*^{Tg}/+ muscles (Extended Data Fig. 5d-5f). On the other hand, genes encoding proteasomal subunits, and *NFE2L1* and *NFE2L2* that activate the proteasomal genes, are transcriptionally upregulated (Extended Data Fig. 5g & 5h). Accordingly, proteasome-associated trypsin-like activity is increased in the *ANT1*^{Tg}/+ muscles (Extended Data Fig.5i). The data support an activation of proteasomal function, which helps preventing the accumulation of ubiquitinated proteins. Fourthly, we found that numerous genes involved in autophagy and

intracellular vesicle trafficking are upregulated in *ANT1*^{Tg}/+ muscles (Fig. 4e & 4f). This includes *SESN2* that is directly activated by the ISR[24].

Finally, we found that the transcription of *CTSL*, encoding the lysosomal cathepsin L protease, is upregulated (Fig. 4g). In parallel, we observed a strong amplification of Lamp2-possitive lysosomes and/or lysosome-derived structures in the *ANT1*^{Tg}/+ muscles (Fig. 4h; Extended Data Fig. 6; Extended Data video 4-5). Transmission electron microscopy revealed many autophagy-related structures of varying morphologies that are absent in WT muscles. Notably, aggresome-like structures were detected in the cytosol of *ANT1*^{Tg}/+ muscles that contain electron-dense material resembling protein aggregates (Fig. 4i). Also detected were multivesicular vacuoles, multilamellar vesicles, flattened multilamellar membranes, and mitophagic and glycophagic bodies (Extended Data Fig. 7 & 8). These observations support hyper-activation of autophagic and lysosomal activities. Collectively, the data strongly support the model that *ANT1* overexpression induces cytosolic protein misfolding/aggregation and mPOS. Muscle cells respond to mPOS by activating multiple proteostatic pathways to rebalance cytosolic proteostasis.

The observation that moderate overloading of the mitochondrial adenine nucleotide carrier is sufficient to cause mPOS was independently confirmed in yeast. We generated a yeast strain that overexpresses *AAC2*, the mammalian homolog of *ANT1*, by 2.2 fold (Extended Data Fig. 9a). Like in *ANT1*^{Tg}/+ muscles, *AAC2*-overexpression reduces mitochondrial respiration (Extended Data Fig. 9b & 9c). *AAC2*-overexpression also reduces cell growth. More importantly, cell growth is inhibited even on the fermentable carbon sources when combined with the disruption of *YME1*, *PHB1* and *PHB2* (Extended Data Fig. 9d). *YME1* encodes the *i*-AAA protein quality control protease on the IMM. Phb1 and Phb2 form the prohibitin complex required for the stabilization of newly synthesized IMM proteins. Disruption of *YME1*, *PHB1* and *PHB2* is known

to cause mPOS[6]. The genetic interactions suggest that *AAC2*-overexpression induces mPOS, which synergizes with *yme1Δ*, *phb1Δ,* and *phb2Δ* to inhibit cell growth. We found that *aac2* alleles with transport-defective mutations also inhibit the growth of *yme1Δ* cells (Extended Data Fig. 9e). mPOS induction by *AAC2*-overexpression is therefore independent of nucleotide transport. Consistent with mPOS, *AAC2*-overexpressing cells cannot tolerate a further proteostatic challenge in the cytosol instigated by the expression of the aggregation-prone human huntingtin protein, Htt(25Q) (Extended Data Fig. 9f). We speculate that Aac2 overloading partially saturates the cytosolic chaperoning system and/or the protein import machinery, which globally reduces mitochondrial protein import and ultimately causes mPOS (Extended Data Fig. 9g). Likewise, moderate *ANT1*-overexpression in mice may also cause mPOS in the *ANT1*^{Tg}/+ muscles by the same mechanism.

In the *ANT1*^{Tg}/+ muscles, we found that the protein content is significantly reduced (Fig. 4k). We propose that chronic proteostatic adaptations to mPOS, which include increased 4EBP expression and eIF2α phosphorylation, and the activation of proteasomal, autophagic and lysosomal functions, converge to cause an imbalance between protein synthesis and degradation (Fig. 4l). Unbalanced protein synthesis and degradation is a known driver of myofiber shrinkage and muscle wasting[8]. In addition to these pro-atrophic pathways, our RNA-Seq analysis also showed that *GADD45A* and *CDKN1A*, two downstream targets of the ISR [25], are upregulated in the *ANT1*^{Tg}/+ muscles (Fig. 4j). *GADD45A* and *CDKN1A* encode the growth arrest and DNA-damage-inducible protein α, and the cyclin-dependent kinase inhibitor 1A (or p21) respectively. Both proteins promote muscle wasting [9, 26]. On the other hand, *FBXO32* and *TRIM63*, encoding the MAFBx/atrogin-1 and MuRF1 ubiquitin ligases that are upregulated in acute models of muscle atrophy[8], are instead down-regulated in *ANT1*^{Tg}/+ muscles (Extended Data Fig. 5j). Thus,

ANT1-induced progressive muscle wasting is mechanistically linked to the chronic activation of adaptive proteostatic programs without the involvement of *FBXO32* and *TRIM63*.

In summary, we found that moderate *ANT1*-overexpression is sufficient to cause progressive muscle wasting. Mitochondrial protein import appears to be readily saturable in the skeletal muscle. Chronic proteostatic adaptation to mitochondrial protein overloading and the resulting mPOS appears to be a robust mechanism of muscle wasting. Protein import is an elaborate process [27]. It is impaired during aging and in those muscle diseases that directly or indirectly affect the import machinery [28, 29]. Our finding could therefore help the understanding of how mitochondrial damage during aging and in import-related diseases affects muscle mass and function. In addition, our work may also have implications for FSHD and dilated cardiomyopathy that are associated with *ANT1* activation [10-12]. FSHD is primarily linked to the ectopic expression in skeletal muscle of *DUX4*, a gene that encodes a transcription factor not normally expressed in somatic tissue [30]. In light of our study, it might be worth reexamining whether or not *ANT1* overexpression contributes to or modifies the course of this disease.

References

1. Batsis, J.A., Mackenzie, T.A., Barre, L.K., Lopez-Jimenez, F. & Bartels, S.J. Sarcopenia, sarcopenic obesity and mortality in older adults: results from the National Health and Nutrition Examination Survey III. *Eur J Clin Nutr* **68**, 1001-1007 (2014).
2. Calvani, R. *et al.* Mitochondrial pathways in sarcopenia of aging and disuse muscle atrophy. *Biol Chem* **394**, 393-414 (2013).
3. Romanello, V. & Sandri, M. Mitochondrial Quality Control and Muscle Mass Maintenance. *Front Physiol* **6**, 422 (2016).
4. Lustgarten, M.S. *et al.* MnSOD deficiency results in elevated oxidative stress and decreased mitochondrial function but does not lead to muscle atrophy during aging. *Aging Cell* **10**, 493-505 (2011).
5. Liu, Y. *et al.* Mitochondrial carrier protein overloading and misfolding induce aggresomes and proteostatic adaptations in the cytosol. *Mol Biol Cell* **30**, 1272-1284 (2019).
6. Wang, X. & Chen, X.J. A cytosolic network suppressing mitochondria-mediated proteostatic stress and cell death. *Nature* **524**, 481-484 (2015).
7. Wrobel, L. *et al.* Mistargeted mitochondrial proteins activate a proteostatic response in the cytosol. *Nature* **524**, 485-488 (2015).
8. Bonaldo, P. & Sandri, M. Cellular and molecular mechanisms of muscle atrophy. *Dis Model Mech* **6**, 25-39 (2013).
9. Ebert, S.M. *et al.* Stress-induced skeletal muscle Gadd45a expression reprograms myonuclei and causes muscle atrophy. *J Biol Chem* **287**, 27290-27301 (2012).

10. Gabellini, D., Green, M.R. & Tupler, R. Inappropriate gene activation in FSHD: a repressor complex binds a chromosomal repeat deleted in dystrophic muscle. *Cell* **110**, 339-348 (2002).

11. Laoudj-Chenivesse, D. *et al.* Increased levels of adenine nucleotide translocator 1 protein and response to oxidative stress are early events in facioscapulohumeral muscular dystrophy muscle. *J Mol Med* **83**, 216-224 (2005).

12. Dorner, A., Schulze, K., Rauch, U. & Schultheiss, H.P. Adenine nucleotide translocator in dilated cardiomyopathy: pathophysiological alterations in expression and function. *Mol Cell Biochem* **174**, 261-269 (1997).

13. Gabellini, D. *et al.* Facioscapulohumeral muscular dystrophy in mice overexpressing *FRG1*. *Nature* **439**, 973-977 (2006).

14. Brand, M.D. *et al.* The basal proton conductance of mitochondria depends on adenine nucleotide translocase content. *Biochem J* **392**, 353-362 (2005).

15. Ibebunjo, C. *et al.* Genomic and proteomic profiling reveals reduced mitochondrial function and disruption of the neuromuscular junction driving rat sarcopenia. *Mol Cell Biol* **33**, 194-212 (2013).

16. Nikkanen, J. *et al.* Mitochondrial DNA Replication Defects Disturb Cellular dNTP Pools and Remodel One-Carbon Metabolism. *Cell Metab* **23**, 635-648 (2016).

17. Bao, X.R. *et al.* Mitochondrial dysfunction remodels one-carbon metabolism in human cells. *Elife* **5** (2016).

18. Kuhl, I. *et al.* Transcriptomic and proteomic landscape of mitochondrial dysfunction reveals secondary coenzyme Q deficiency in mammals. *Elife* **6** (2017).

19. Pakos-Zebrucka, K. *et al.* The integrated stress response. *EMBO Rep* **17**, 1374-1395 (2016).

20. Baker, B.M., Nargund, A.M., Sun, T. & Haynes, C.M. Protective coupling of mitochondrial function and protein synthesis via the eIF2alpha kinase GCN-2. *PLoS Genet* **8**, e1002760 (2012).

21. Lin, Y.F. & Haynes, C.M. Metabolism and the UPR(mt). *Mol Cell* **61**, 677-682 (2016).

22. Weidberg, H. & Amon, A. MitoCPR-A surveillance pathway that protects mitochondria in response to protein import stress. *Science* **360** (2018).

23. Juliana, C.A. *et al.* ATF5 regulates beta-cell survival during stress. *Proc Natl Acad Sci U S A* **114**, 1341-1346 (2017).

24. Garaeva, A.A., Kovaleva, I.E., Chumakov, P.M. & Evstafieva, A.G. Mitochondrial dysfunction induces SESN2 gene expression through Activating Transcription Factor 4. *Cell Cycle* **15**, 64-71 (2016).

25. Adams, C.M., Ebert, S.M. & Dyle, M.C. Role of ATF4 in skeletal muscle atrophy. *Curr Opin Clin Nutr Metab Care* **20**, 164-168 (2017).

26. Bongers, K.S. *et al.* Skeletal muscle denervation causes skeletal muscle atrophy through a pathway that involves both Gadd45a and HDAC4. *Am J Physiol Endocrinol Metab* **305**, E907-915 (2013).

27. Chacinska, A., Koehler, C.M., Milenkovic, D., Lithgow, T. & Pfanner, N. Importing mitochondrial proteins: machineries and mechanisms. *Cell* **138**, 628-644 (2009).

28. Szczesny, B., Hazra, T.K., Papaconstantinou, J., Mitra, S. & Boldogh, I. Age-dependent deficiency in import of mitochondrial DNA glycosylases required for repair of oxidatively damaged bases. *Proc Natl Acad Sci U S A* **100**, 10670-10675 (2003).

29. Vukotic, M. *et al.* Acylglycerol Kinase Mutated in Sengers Syndrome Is a Subunit of the TIM22 Protein Translocase in Mitochondria. *Mol Cell* **67**, 471-483 e477 (2017).

30. Statland, J.M. & Tawil, R. Facioscapulohumeral muscular dystrophy: molecular pathological advances and future directions. *Curr Opin Neurol* **24**, 423-428.

Supplemental Information contains supplementary table 1-3 and video 1-5.

Acknowledgments: We thank David Mitchell for help on electron microscopy, Siu-Pok Yee (University of Connecticut) for the generation of the *ANT1*-transgenic mice, Don Henderson (University of Rochester) and Christopher Turner for muscle histology, Jushuo Wang for confocal microscopy, the Chen laboratory members for comments on the manuscript, SUNY Upstate Medical University Department of Laboratory Animal Resources for animal care, and Vanderbilt University Mouse Metabolic Phenotyping Center (MMPC) for mouse phenotyping. This work was supported by the NIH grants AG061204 and AG047400 to X.J.C..

Author Contributions X.W., X.J.C. and R.T. performed the experiments. F.M. processed and analyzed the RNA-Seq data. X.W. and X.J.C. wrote the manuscript.

The authors declare no competing financial interests.

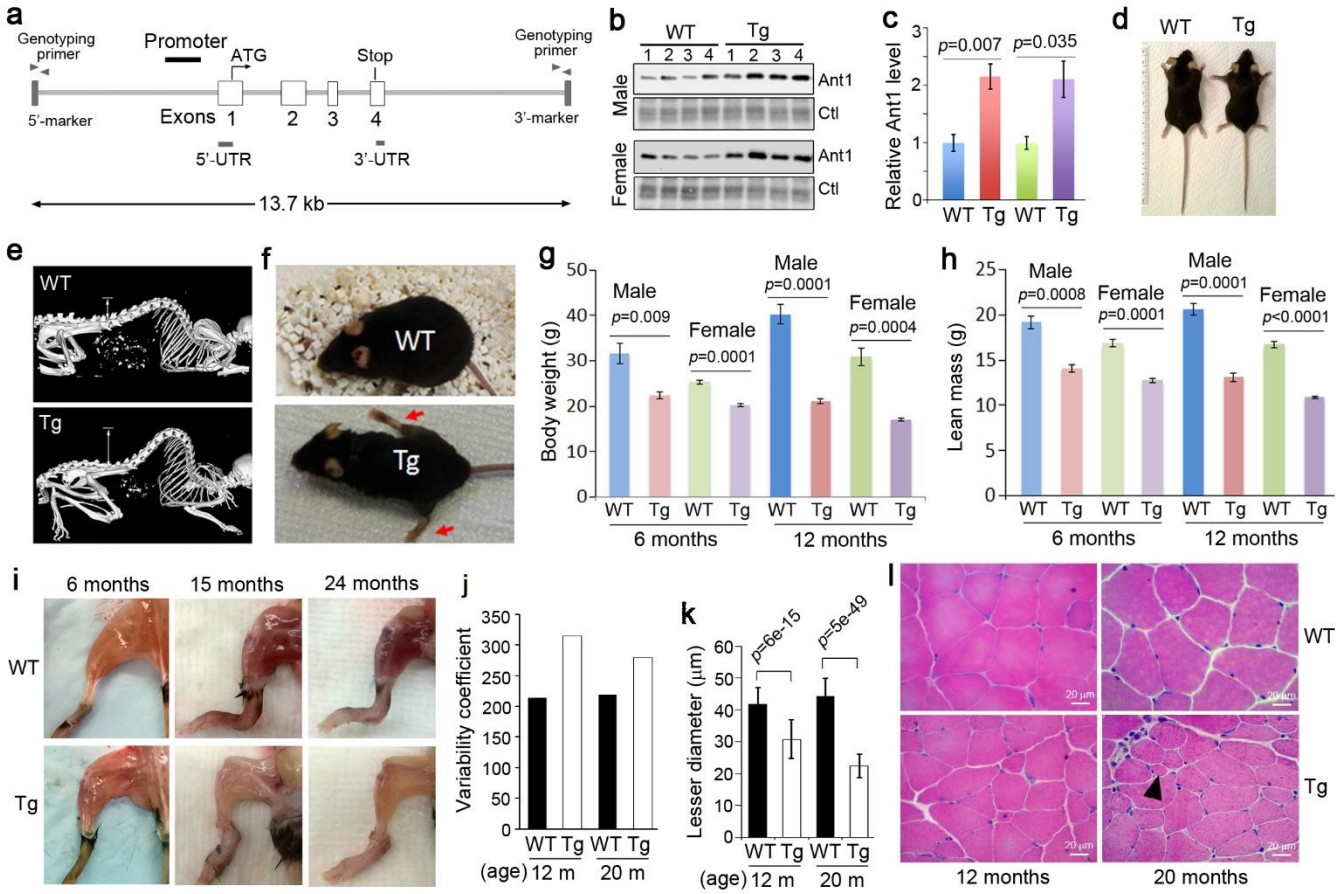

Figure 1. **Moderate *ANT1*-overexpression causes progressive muscle wasting**. (**a**) Schematic showing the genomic clone of the mouse *ANT1* gene, which was used to generate *ANT1*-transgenic mice. (**b**) and (**c**) Steady state levels of Ant1 in quadriceps muscle from transgenic (Tg) and wild-type (WT) littermates (n=4) at the age of 6 months, as determined by western blot. Ctl, total protein control. (**d**) Body length at 6 months. (**e**) Micro-CT scanning at 6 months. (**f**) Gait abnormalities at 19 months. (**g**) and (**h**) Body weight and lean mass at 6 and 12 months (n=4/sex/genotype). (**i**) Progressive muscle wasting. (**j**) Myofiber variability coefficient at the age of 12 and 20 months (quadriceps). m, month. (**k**) Lesser diameters of muscle fibers (quadriceps). (**l**) H&E staining of quadriceps muscles. Arrowhead denotes a rounded small myofiber. Error bars represent S.E.M. and *p* values were calculated by unpaired Student's *t* test.

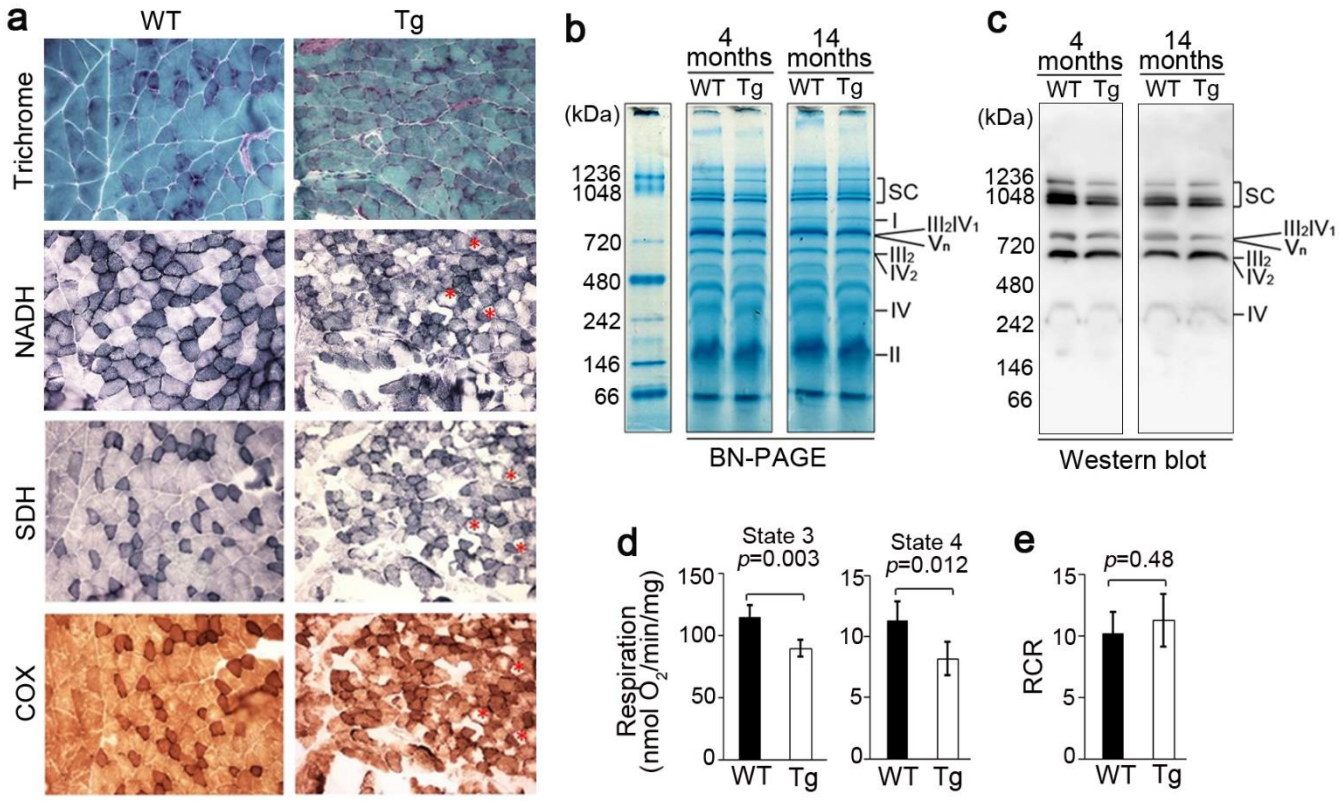

Figure 2. Histological and bioenergetic analyses of *ANT1^{Tg}*/+ muscles. (**a**) Histology of gastrocnemius muscles from 8.5-month-old *ANT1^{Tg}*/+ and control mice by modified Gomori Trichrome, NADH, SDH and COX staining. Moth-eaten myofibers are marked by asterisks. (**b**) BN-PAGE analysis of quadriceps mitochondria from 4- and 14-month-old mice. SC, supercomplexes. I – V, respiratory complexes I – V. (**c**) Western blot analysis of samples used in (b) using antibodies against respiratory complexes. (**d**) Mitochondrial respiratory rates of skeletal muscle mitochondria. Error bars represent standard deviations of four measurements of mitochondria isolated from one pair of 4-month-old mice. (**e**) Respiratory control ratio (RCR).

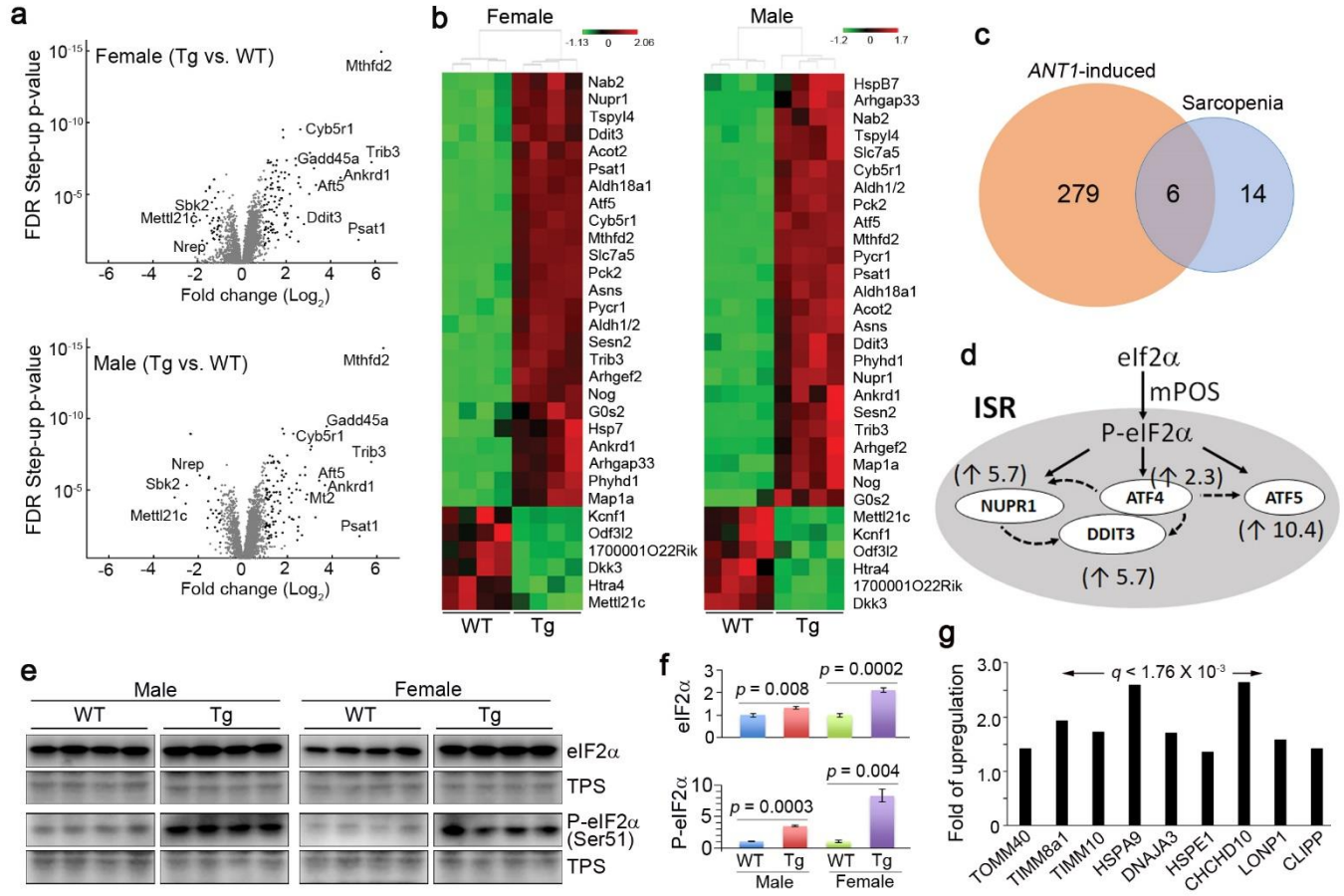

Figure 3. **Cytosolic adaptive responses to *ANT1*-overexpression**. (**a**) Volcano plots showing the distribution of up- and down-regulated genes in quadriceps muscle from female (n=4/genotype) and male (n=4/genotype) mice at the age of 6 months (two-way ANOVA, $q < 0.05$). Genes with >2 fold changes ($p<0.05$) in transcription are highlighted in bold. (**b**) Heatmaps showing genes that are commonly up- and down-regulated in the *ANT1*-transgenic female and male mice by >5 fold. (**c**) Venn diagram showing a partial overlap between the top 20 upregulated genes in sarcopenia [15] and the 285 genes in *ANT1*-transgenic mice upregulated by >1.5 fold. (**d**) The upregulation of ISR genes in *ANT1*-transgenic muscles. Fold changes in transcription are indicated in the parentheses. Solid lines represent translational activation and dashed lines denote transcriptional activation. (**e**) and (**f**) Increased phosphorylation of eIF2α in *ANT1*-transgenic muscles, as determined by western blot. TPS, total protein staining. (**g**) Upregulation of genes involved in mitochondrial protein import and proteostasis.

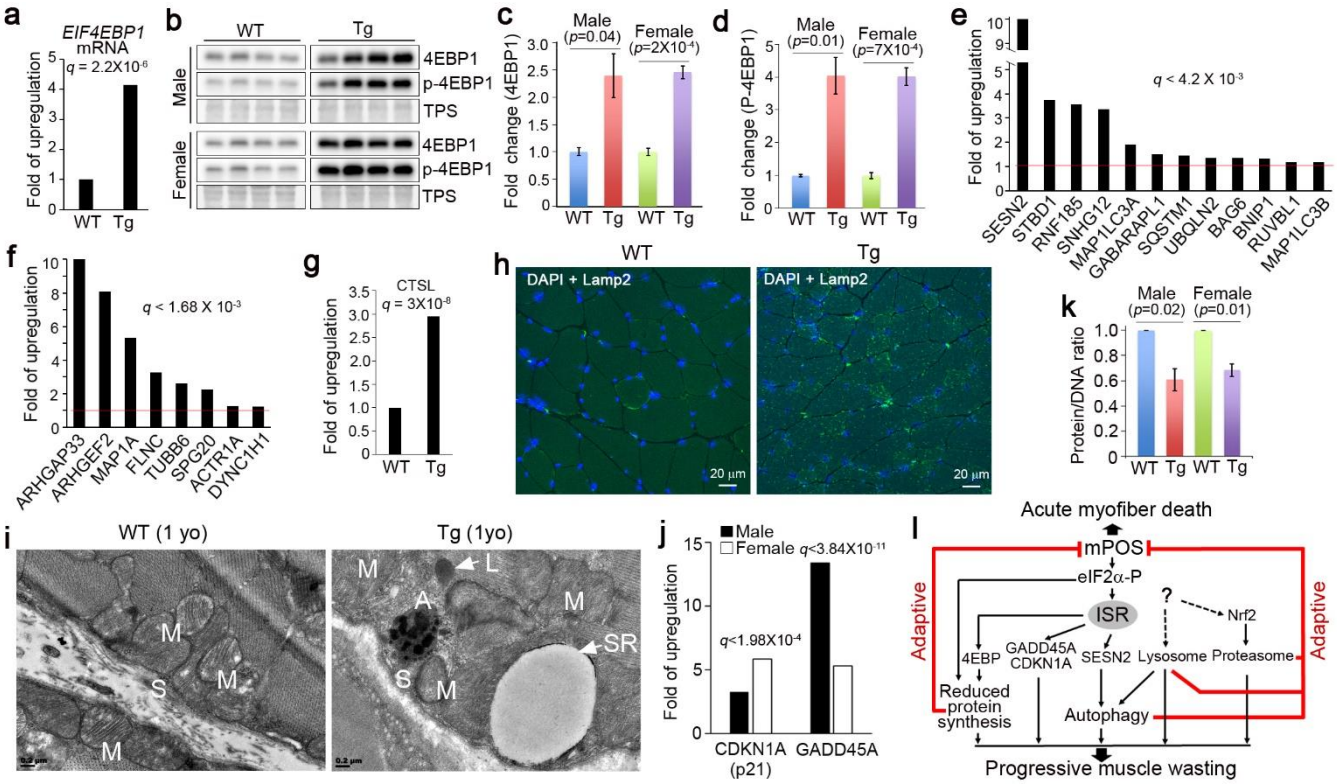

Figure 4. Proteostatic remodeling in the cytosol in response to *ANT1*-overexpression. (**a**) Transcriptional activation of *EIF4EBP1*. (**b** – **d**) Upregulation of 4EBP1 protein and its phosphorylated form, P-4EBP1, as determined by western blot. (**e**) Transcriptional upregulation of genes involved in autophagy. (**f**) Transcriptional upregulation of genes involved in vesicle trafficking. (**g**) Transcriptional upregulation of *CTSL* encoding the lysosomal cathepsin L protease. (**h**) Immunofluorescence detection of Lamp2 in cross-sections of quadriceps from *ANT1*-transgenic and control mice at 12 months of age. Blue, DAPI-stained nuclei; green, Lamp2-positive structures. (**i**) Transmission microscopy showing the aggresome-like structures in the *ANT1*-transgenic quadriceps muscles from one-year-old mice. A, aggresome-like structure; L, lysosome; M, mitochondria; S, sarcolemma; SR, dilated sarcoplasmic reticulum. (**j**) Transcriptional upregulation of *GADD45A* and *CDKN1A* in *ANT1*-transgenic muscles. (**k**) Protein/DNA ratio in six-month-old quadriceps muscles (n=4 for both males and females). (**l**) A model for mPOS-induced proteostatic adaptations that unbalance protein synthesis and degradation, which ultimately causes progressive muscle wasting as an undesired trade-off. Red lines represent adaptive processes to counteract mPOS and the dashed line denotes an unknown transcriptional activation mechanism. Error bars represent S.E.M.. *P* values were calculated by unpaired Student's *t* test.

METHODS

Antibodies for western blot and immunofluorescence analysis. Antibodies used in this study included the Total OXPHOS Human WB Antibody Cocktail (#ab1104a1, Abcam), anti-Ant1 (#SAB2108761, Sigma), anti-Bax (#ab32503, Abcam), anti-eIF2α (#9722, Cell Signaling), anti-phospho-eIF2α (Ser51) (#3597, Cell Signaling), anti-4EBP1 (#9644, Cell Signaling), anti-Lamp2 (#GL2A7, Developmental Studies Hybridoma Bank, University of Iowa), anti-phospho-4EBP1 (#2855, Cell Signaling), anti-p62 (#23214, Cell Signaling), anti-rpS6 (#ab40820, Abcam), anti-phospho-rpS6 (#ab65748, Abcam), anti-ubiquitin (#701339, Thermo Scientific). Total proteins were stained with REVERT Total Protein Stain (#926-11011, LI-COR). For western blot, band intensities were quantified by the LI-COR Odyssey Fc Imaging system and normalized against total protein staining.

Yeast strains and growth media. All the *Saccharomyces cerevisiae* strains used are derived from the BY4741/BY4742 background. The *GAL10-AAC2* cassette was integrated into the chromosome and *AAC2* expression was induced in complete medium containing 2% galactose (Gal) and 2% raffinose (Raf). To test *AAC2* toxicity, the wild-type and mutant *AAC2* alleles were expressed from the multicopy vector pRS425 (LEU2). The plasmids were introduced into *yme1Δ* cells by LiAc-mediated transformation. The transformed cells were plated onto minimal glucose medium lacking leucine and selected for Leu^+ colonies after incubating at 30˚C for three days. To test the synthetic growth defect between *AAC2* and *HTT(25Q)*, the strain BY/GAL-AAC2 (*GAL10-AAC2*) was transformed with a *URA3*-based plasmid expressing *HTT(25Q)* under the control of the *GAL10* promoter. The Ura^+ transformants were selected on minimal glucose medium lacking uracil, and were then tested on minimal galactose medium lacking uracil for growth at 25°C for four days.

Generation of *ANT1*-transgenic mice. The Ant1 transgene was prepared by recombineering according to Lee et al.[31]. Briefly, genomic sequences corresponding to Ant1 5' upstream and 3' downstream genomic sequence were prepared by PCR using primer pairs ret5F (5'- GTCGAATTC GTATATAAATAAATAAAAGAAAG) and ret5R (5'- GTCAGACGTC CAATGTTGCTACTTAAACACTCTTG) and ret3F (5' GTCA GACGTC CCTTGAGAACTAACACAGAGCAG) and ret3R (5' GTCAAAGCTT GGTGATATGGGGACAGGAAGGAG). The 5' and 3' mini-arms were digested with *Eco*RI and *Aat*II, and *Hin*dIII and *Aat*II, respectively, and then inserted into pSK+. The mini-arm vector was then digested with *Aat*II, treated with phosphatase, and then electroporated into EL350 together with a BAC clone, RP24-108A1, which contains the entire Ant1 genomic sequence, to retrieve Ant1 genomic sequence from the BAC by gap repair. The retrieved Ant1 genomic sequence is 13.7 kb in size containing all 4 exons together with 4.2 kb and 4.96 kb of 5' up- and 3' down-stream sequences, respectively. The Ant1 transgene fragment was released from the plasmid by *Not*I and *Kpn*I digestion, fractionated by agarose gel electrophoresis, column purified and resuspended in 10mM Tris, pH8.0.

ANT1-transgenic mice were generated according to Nagy et al.[32]. Briefly, four to six week old C57BL6j females were superovulated by first adminstration of 5 IU of pregnant mare serum (PMS) and 44 to 46 hour later with 5 IU human chorionic gonadotropins (HCG). The females are then mated with C57BL6j stud males. Fertilized one-cell embryos were collected from the oviduct the next day and maintained in KSOM medium in an air/CO_2 incubator at 37°C until use. Purified Ant1 genomic fragment were diluted to approximately 1 ng/μl and then microinjected into the pronuclei of the one-cell embryos. Injected embryos were implanted into the oviducts of 0.5 days

post coitium pseudopregnant females for subsequent development *in utero*. Transgenic mice were identified by PCR using genomic DNA prepared from ear notch as template. Two primer pairs specific to the 5' and 3' end of the Ant1 transgene were used for genotyping. Primer pair BHtoRI (5'- GGATCCCCCGGGCTGCAGGAATTC) and Ant R5 (5'- CAATGTTGCTACTTAAACACTCTTG), corresponds to the 5' will identify a fragment of 515 bp, and a second pair of primers, XhotoHind (5'- GAGGTCGACGGTATCGATAAGCTTG) and AntR3F (5'-CTTTCCTGGACCCCTGTAAGCTTG) will detect a fragment of 432 bp specific to the 3' end of the transgene. Founder animals were then mated with C57BL6NTac mice to establish and maintain the transgenic line. All the animal experiments have been approved by the Institutional Animal Care and Use Committee (IACUC) of the State University of New York Upstate Medical University. The experiments were performed using age-matched and mostly littermate controls. The animals were fed with a regular chow diet *ad libitum* and were housed at an ambient temperature. Food and water were placed at a low and reachable position for the *ANT1*-transgenic mice over one-year-old.

Lean mass, home cage activity and exercise endurance tests. Lean mass and home cage activity were measured by quantitative magnetic resonance and Promethion metabolic caging respectively at Vanderbilt University Mouse Metabolic Phenotyping Center. Exercise endurance was measured with an Exer 3/6 Treadmill (Columbus Instruments) by determining the maximum distance and speed of the animals before exhaustion. The animals were trained for at least two sessions before the tests.

Mitochondrial isolation and bioenergetic assay. Unanesthetized mice were decapitated using a guillotine. Muscle mitochondria were isolated according to Garcia-Cazabin et al. [33]. Oxygen consumption rates were measured using an Oxygraph Plus oxygen electrode (Hansatech Instruments Ltd), with 150 μg mitochondria, 5 mM glutamate, 2.5 mM malate, 150 μM ADP. Oligomycin (5 μg/ml) was added to established state-4 respiration. Respiratory control ratio was established by dividing state-3 respiratory rate with oligomycin-inhibited respiratory rate.

Muscle histology and immunohistochemistry. Standard procedures were followed for H&E, Trichrome, NADH, SDH and COX activity staining, and for the determination of lesser diameter and variability coefficient of muscle fibers [34]. For immunofluorescence microscopy, muscle sections of 10 μm thickness were fixed and permeabilized with 100% methanol at -20°C for 15 minutes, rinsed in PBS, treated in blocking buffer (1XPBS/5% Normal Goat Serum/0.3% Triton X-100) for one hour at room temperature, followed by incubation with anti-Lamp2 antibody at 4˚ C overnight. The specimens were then washed in 1XPBS/0.1% Tween 20 before being probed with an Alexa Fluor 488-conjugated anti-rat IgG (H+L) antibody for one hour at room temperature. After washing with 1XPBS/0.1% Tween 20, the tissue samples were mounted with ProLong Diamond Antifade Mountant with DAPI (#P36962, Invitrogen), and were visualized using a Leica SP8 confocal microscope.

Electron microscopy. Fresh muscle samples were fixed in 4% glutaraldehyde/0.1 M cacodylate buffer, pH7.2 at room temperature for two hours, and postfixed with 1% osmium tetroxide/0.1 M cacodylate buffer, pH7.2 at room temperature for one hour. The specimens were dehydrated in 50%, 70%, 90%, 100% ethanol and propylene oxide, before being embedded in Luft's Araldite

502 embedding medium (Electron Microscopy Sciences, Hatfield, PA) and cut into thin sections. The ultrathin sections were then stained with ethanolic uranyl acetate and Reynold's lead citrate (Polysciences). The samples were examined with a JOEL JEM1400 transmission electron microscope and images were acquired with a Gaten DAT-832 Orius camera.

RNA-Seq analysis. Total RNA was extracted from snap-frozen quadriceps muscles (n=4/genotype/sex) using RNeasy mini kit (Qiagen). The quality of total RNA was validated by Bioanalyzer (Agilent Technologies). Approximately 1 μg of RNA per sample was used to construct the cDNA library using TruSeq stranded mRNA library prep kit (Illumina). The cDNA libraries were quantitated using KAPA library quantification kit for Illumina platforms (Kapa Biosystems). The individual indexed libraries were diluted to 4 nM and pooled in equal quantity, denatured before loading onto the Illumina NextSeq 500. The sequencing was run as paired-end reads (2 × 75 bp per read) with a targeted depth of 60 million paired-end reads per sample. After sequencing, reads were aligned to build mm10 of the mouse genome using Bowtie2. PartekFlow (Partek, Inc., St. Louis, MO) was used for quantification to RefSeq89 with the EM algorithm and normalization was performed with the Reads Per Kilobase per Million mapped reads (RPKM) method. A two-way (genotype x sex) analysis of variance (ANOVA) was initially used to test for possible differences in expression, with the q value set at $q < 0.05$ for false discovery rate (FDR) correction. This was followed by separate one-way ANOVAs for males and females with the same FDR threshold applied in each case.

Determination of protein/DNA ratio. DNA and proteins were extracted from approximately 30 of quadriceps muscles using AllPrep DNA/RNA/Protein Mini kit (#80004, Qiagen). DNA

concentrations were determined by Thermo Scientific NanoDrop 2000c spectrophotometer. Protein concentrations were determined by Bradford protein assay (#5000006, Bio-Rad). Relative protein contents in the muscles were calculated after normalizing by total amount of DNA.

Proteasomal activity assay. Quadriceps muscle samples (1 mg) were sonicated in PBS plus EDTA (5 mM, pH 7.4) buffer three times for 5 seconds with 25 seconds intervals on ice. After the removal of cell debris by centrifugation, protein concentration of the soluble fractions was determined by Bradford assay. 10 μg of the muscle lysates were used for determining proteasome-associated chymotrypsin-like activity with the Proteasome-Glo™ Assay Systems (#G8531, Promega). Luminescence signals were detected with the SpectraMax i3x Multi-Mode Microplate Reader (Molecular Devices) between 10–30 minutes at room temperature after the addition of luminogenic substrates. The chymotrypsin-like activity were calculated by subtracting MG132 (50 μM)-inhibited activities from total activity.

Data deposition. All raw FastQ files and processed read alignment count data from the RNA-Seq experiments have been deposited into the NCBI Gene Expression Omnibus/Sequence Read Archive (accession number: GSE135584).

Reference:

31. Lee, E.C. *et al.* A highly efficient Escherichia coli-based chromosome engineering system adapted for recombinogenic targeting and subcloning of BAC DNA. *Genomics* **73**, 56-65 (2001).

32. Nagy, A., Gertsenstein, M., Vintersten, K. & Behringer, R. *Manipulatiing the Mouse Embryo: A Laboratory Manual*, Edn. 3. (Cold Spring Harbor Laboratory Press, New York; 2003).

33. Garcia-Cazarin, M.L., Snider, N.N. & Andrade, F.H. Mitochondrial isolation from skeletal muscle. *J Vis Exp* (2011).

34. Dubowitz, V., Lane, R. & Sewry, C.A. *Muscle Biopsy: A Pratical Approach*, Edn. 3rd ed. (Saunders Elsevier, Philadelphia, PA; 2007).

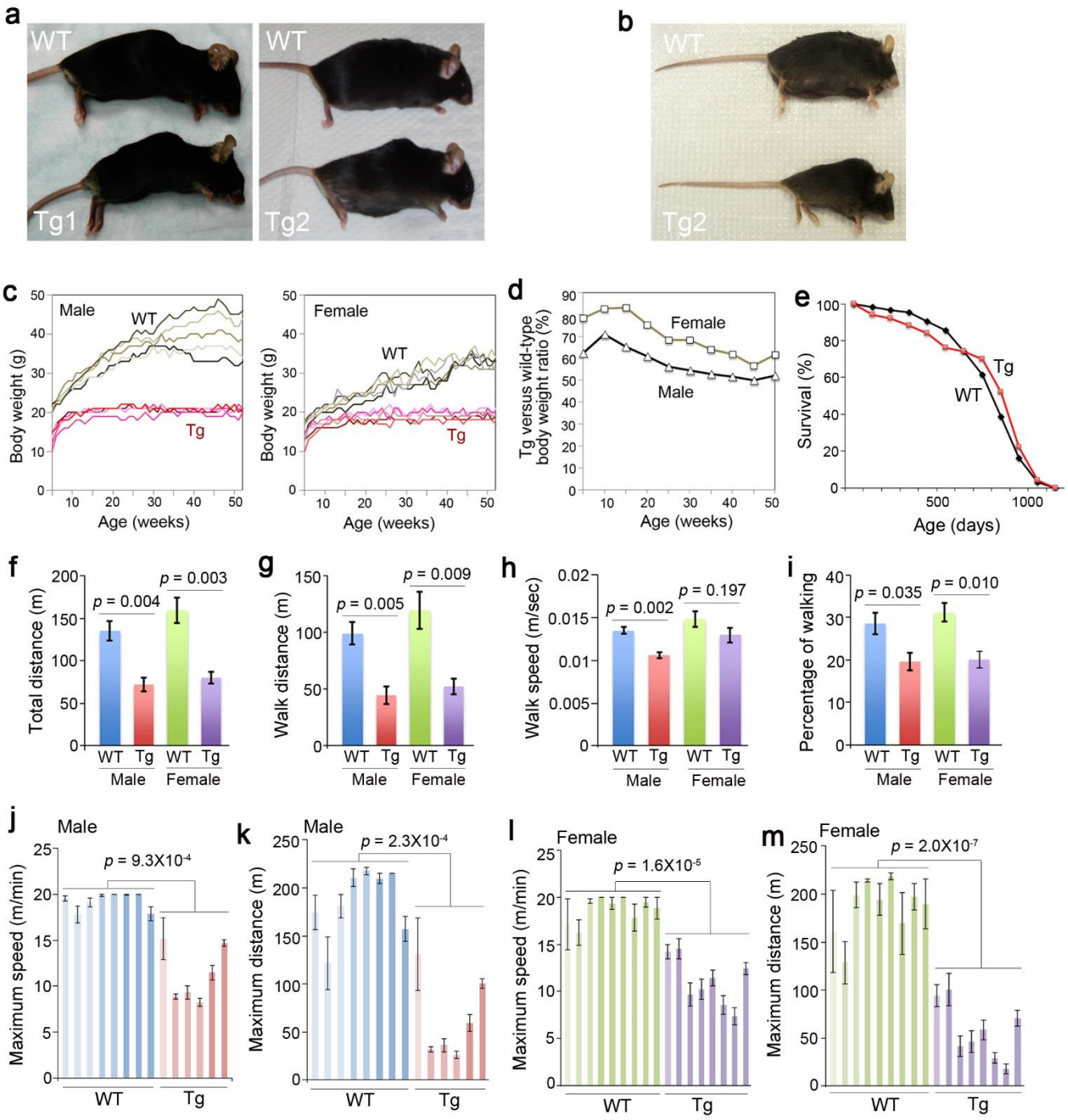

Extended Data Figure 1. **Body morphology, weight, lifespan, home cage activity and exercise endurance of *ANT1^{Tg}*/+ mice compared with wild-type controls.** (**a**) Kyphotic phenotype in two independent *ANT1^{Tg}*/+ lines at the age of 3 (left) and 6 (right) months respectively. (**b**) Kyphotic phenotype of *ANT1^{Tg}*/+ mice at 17 months. (**c**) and (**d**) Body weight of *ANT1^{Tg}*/+ mice (n=5). (**e**) Lifespan of *ANT1^{Tg}*/+ mice (n=50) compared with wild-type controls (n=62). (**f-i**) Home cage activity of one-year-old *ANT1^{Tg}*/+ and littermate control mice in the dark cycle (n=4/genotype/sex). Note that we found no significant differences in home cage activity between *ANT1^{Tg}*/+ and control mice in the light

cycle. Error bars represent S.E.M. and *P* values were calculated by unpaired Student's *t* test. (**j-m**) Exercise endurance of *ANT1*^{Tg}/+ mice compared with littermate controls (6.5-8.5 months old; n=6-9/sex). The maximum speed and distance of wild-type mice were not tested beyond 20 m/min and 200 m respectively. Note that the *ANT1*^{Tg}/+ mice have significant decreases compared with control mice in all the activity parameters measured, except for female *ANT1*^{Tg}/+ mice that have only a marginally reduced walk speed compared with wild-type. Error bars represent S.E.M. of 4-6 tests for each mouse. *P* values were calculated by unpaired Student's *t* test.

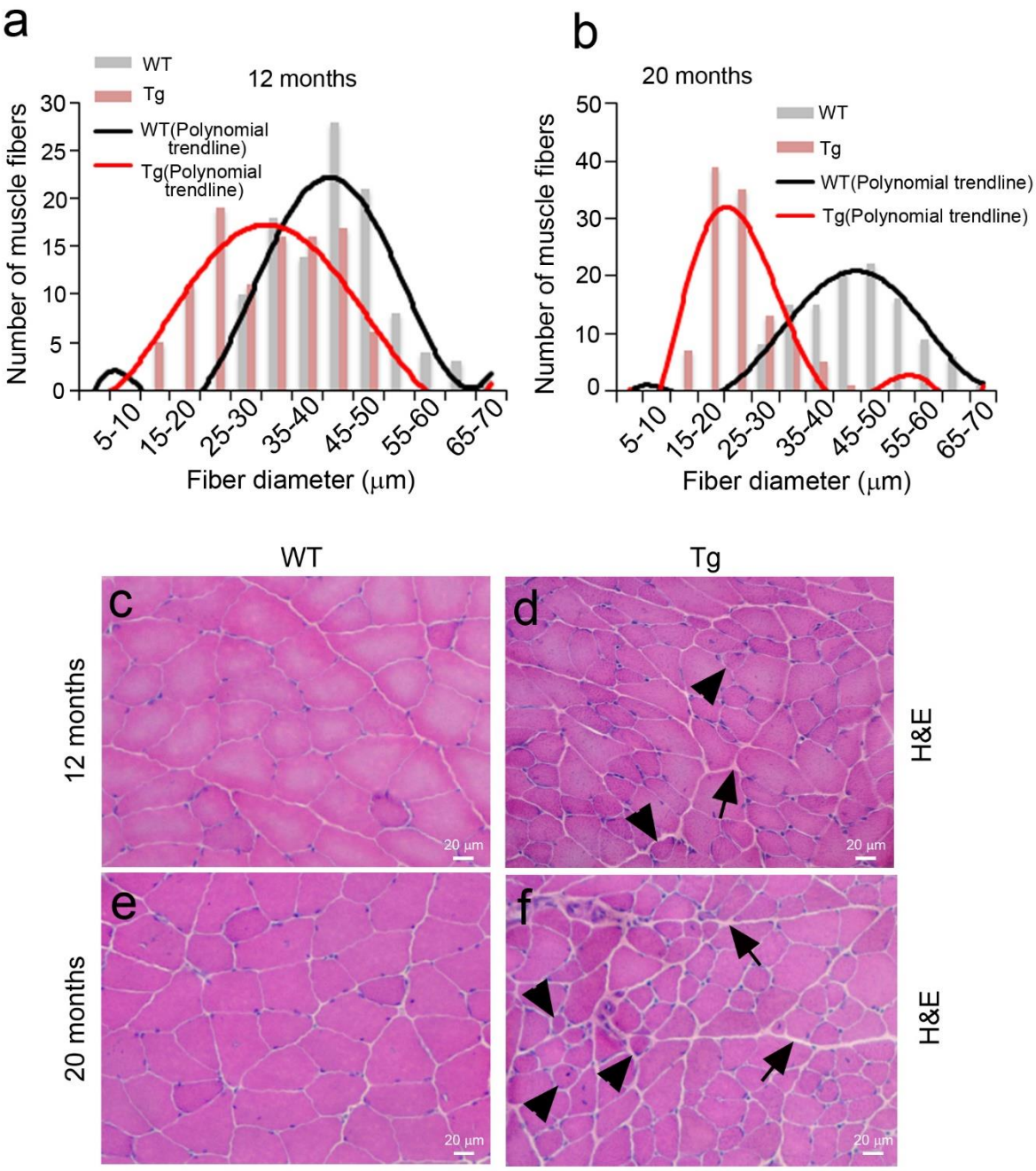

Extended Data Figure 2. **Histological analysis of *ANT1^{Tg}*/+ muscles. (a)** and **(b)** Muscle fiber size distribution at the age of 12 and 20-month-old female mice, respectively. (**c**) – (**f**), hematoxylin and eosin (H&E) staining of *ANT1^{Tg}*/+ quadriceps muscles compared with wild type controls. Arrows and arrow heads denote endomyosium and round-shaped small myofibers, respectively.

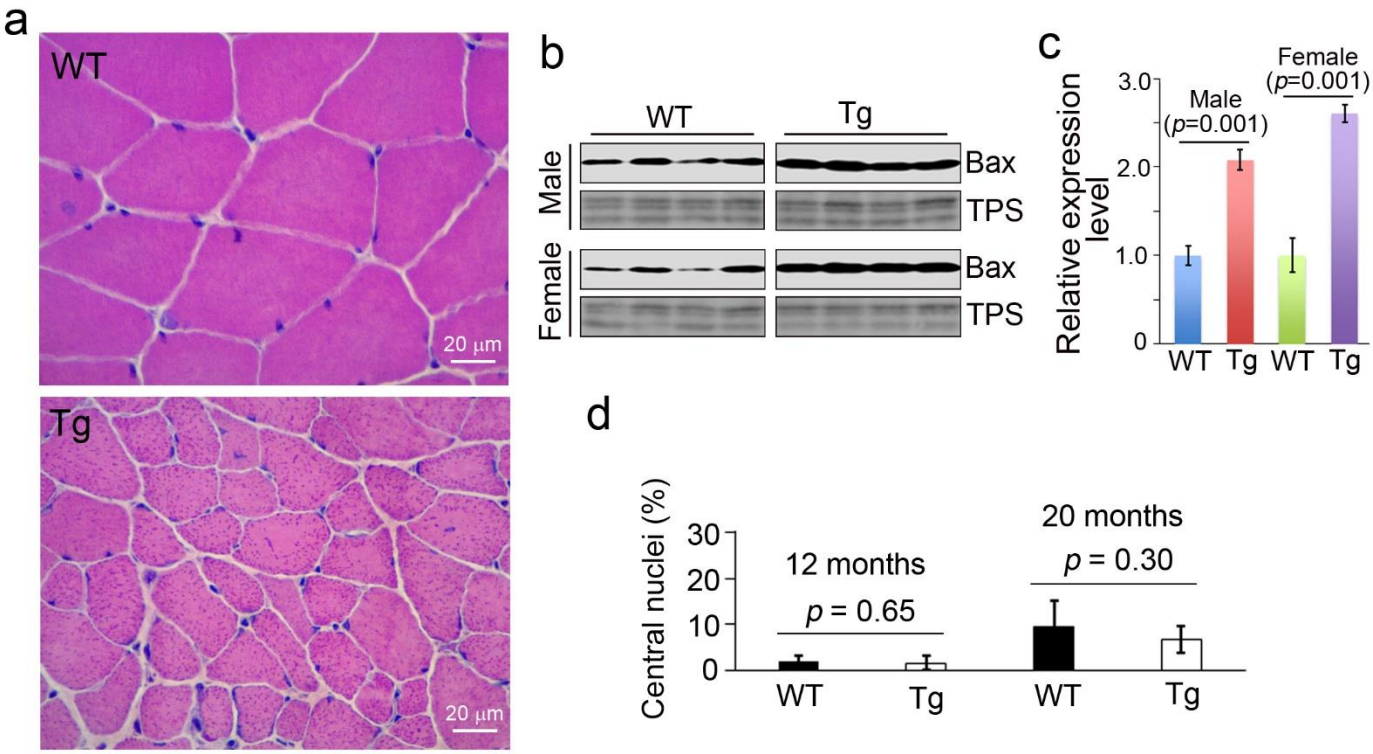

Extended Data Figure 3. **Basophilic structures, *BAX* expression and nuclear positioning in *ANT1^{Tg}*/+ muscles.** (**a**) H&E staining of quadriceps showing basophilic stippling in a 20-month-old female *ANT1^{Tg}*/+ mouse. (**b**) and (**c**) Increased steady state levels of Bax in male and female *ANT1^{Tg}*/+ mice (n=4 each), as measured by western blot. (**d**) Myofibers with central nuclei in *ANT1^{Tg}*/+ and control mice at the age of 12 and 20 months. Totally 296 - 451 myofibers from 5-8 different fields were counted at each time point.

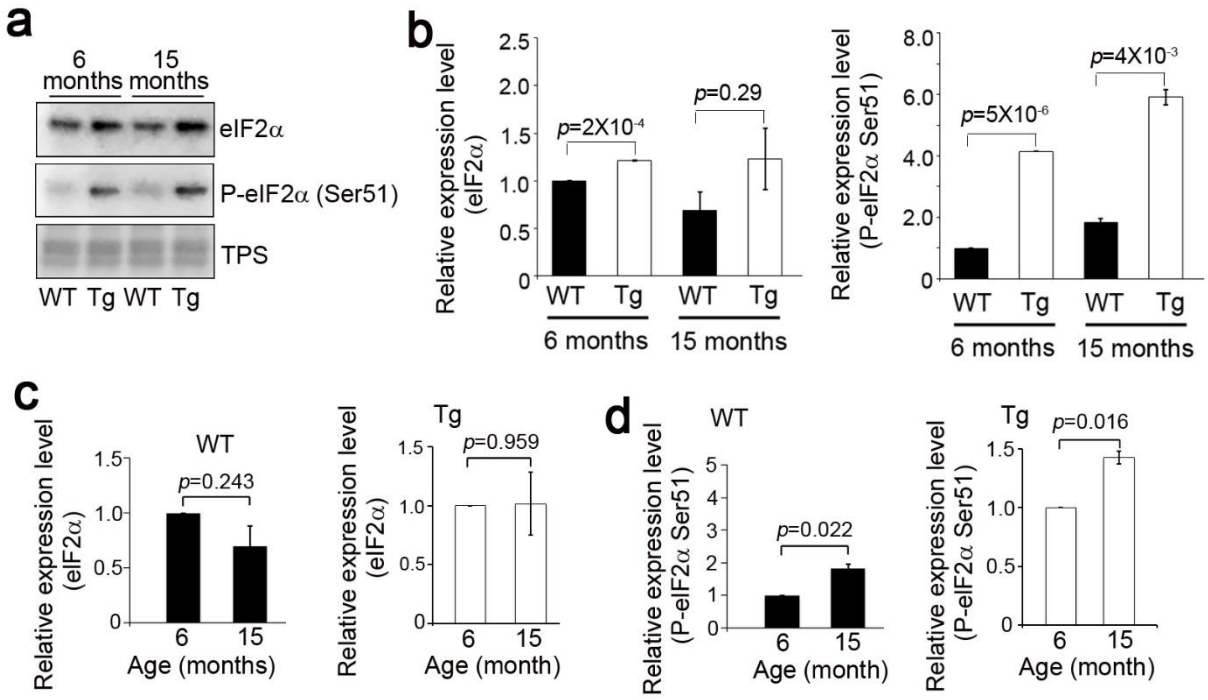

Extended Data Figure 4. **Increased phosphorylation of eIF2α in *ANT1^{Tg}*/+ and wild-type mice during aging.** (**a**) Western blot showing the levels of eIF2α and its phosphorylated form, P-eIF2α (Ser51), in *ANT1^{Tg}*/+ and wild-type male mice at 6 and 15 months of age. (**b**) Comparison between *ANT1^{Tg}*/+ and wild-type mice. (**c**) and (**d**) Comparison eIF2α and P-eIF2α (Ser51) levels at different ages.

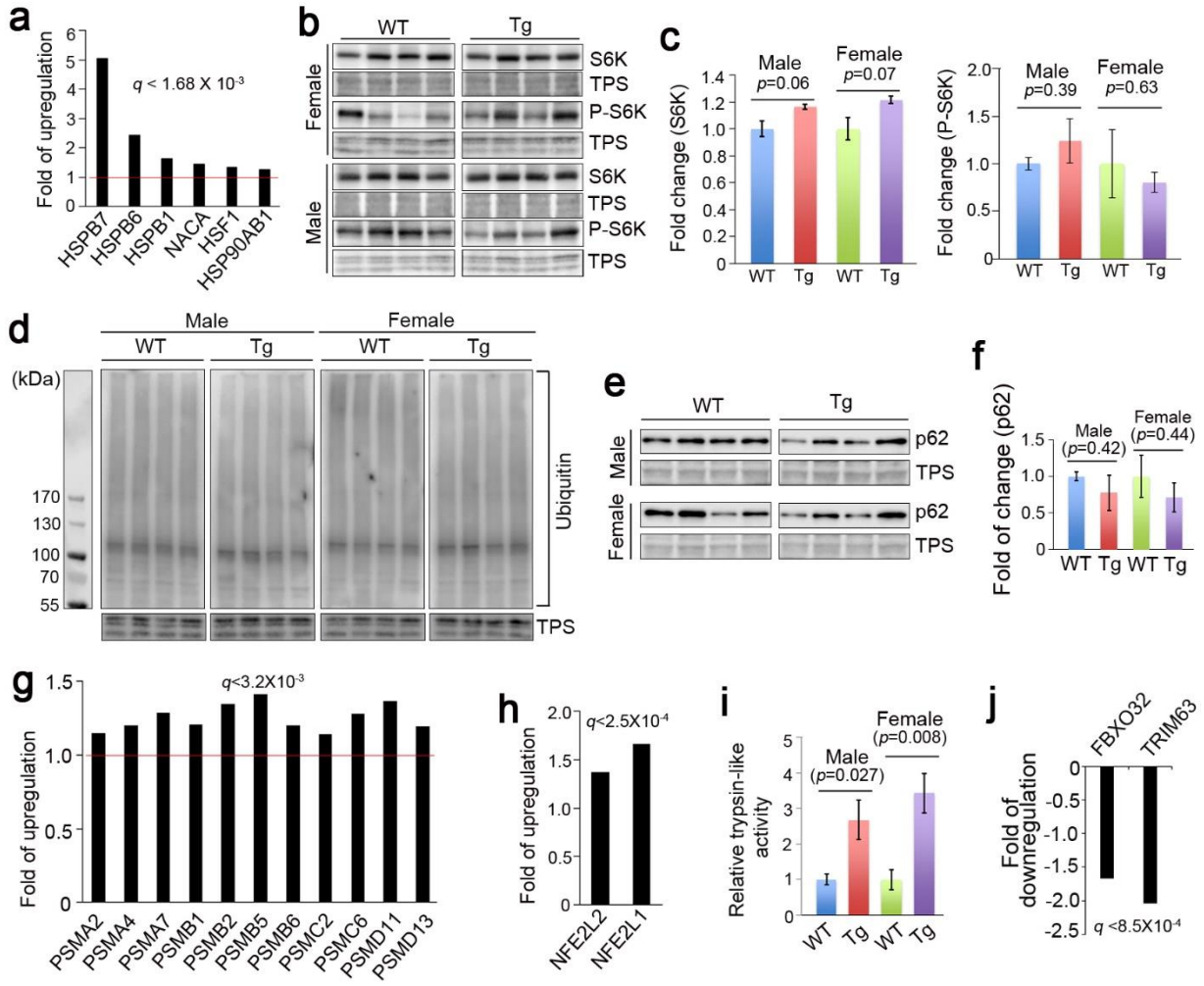

Extended Data Figure 5. **Cytosolic proteostatic adaptations in *ANT1^{Tg}*/+ mice.** (**a**) Transcriptional upregulation of heat shock and chaperone proteins. (**b**) and (**c**) The phosphorylation state of rpsS6 kinase (S6K), as measured by western blot. (**d**) Western blot showing ubiquitinated proteins using an anti-ubiquitin antibody. (**e**) and (**f**) Steady state levels of p62, as determined by western blot. (**g**) Upregulation of genes encoding proteasomal subunits. (**h**) Transcriptional upregulation of *NFE2L2* and *NFE2L1*. (**i**) Trypsin-like activity associated with the proteasome in *ANT1^{Tg}*/+ quadriceps muscles at the age of six months. Error bars represent S.E.M. of four male and female mice with four measurements from each mouse. (**j**) Transcriptional down-regulation of *FBXO32* and *TRIM63* (n=4/sex). Error bars represent S.E.M. and *p* values were calculated by unpaired Student's *t* test.

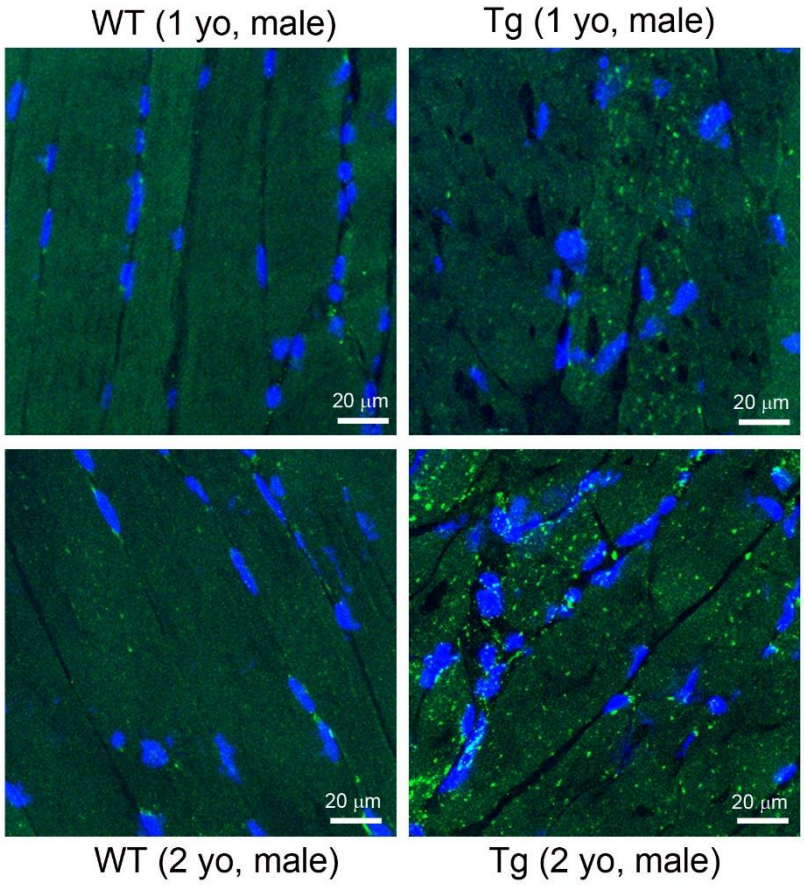

Extended Data Figure 6. **Confocal microscopy showing Lamp2-positive lysosomal and lysosome-associated cellular structures in quadriceps muscles from *ANT1*^{Tg}/+ and control mice.** Longitudinal sections were examined in one- and two-year-old male mice. Blue, DAPI-stained nuclei; green, Lamp2-positive structures.

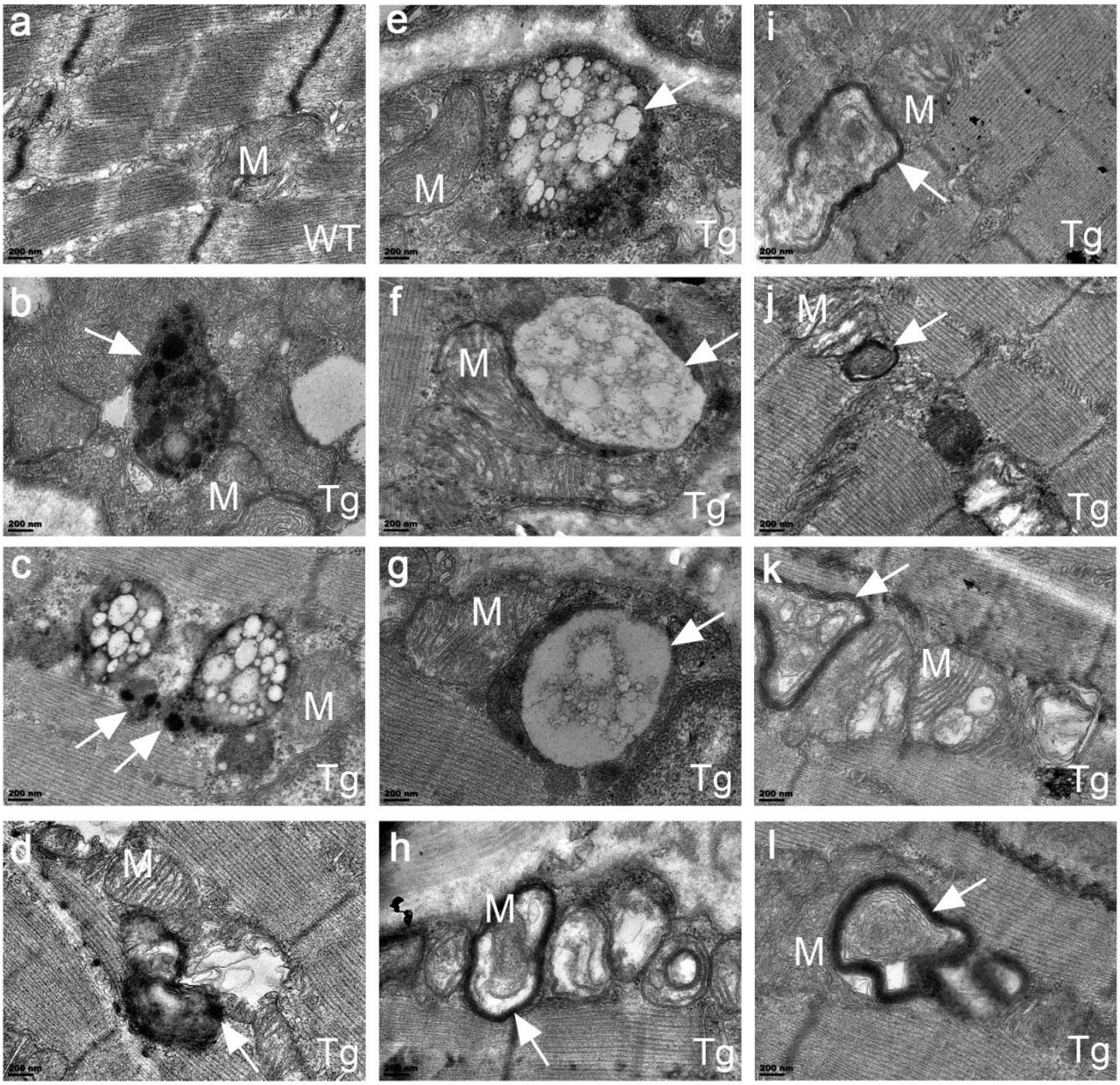

Extended Data Figure 7. **Transmission electron microscopy of quadriceps muscles from one-year-old wild-type (WT, panel a) and *ANT1*^{Tg}/+ (Tg, panels b-l) mice.** M, mitochondria; Arrows denote aggresome/lysosome-like structures that contain electron-dense aggregates (b-d), multivesicular vacuoles (e-g), mitophagic vacuoles (h), and multilamellar vesicles (i-l).

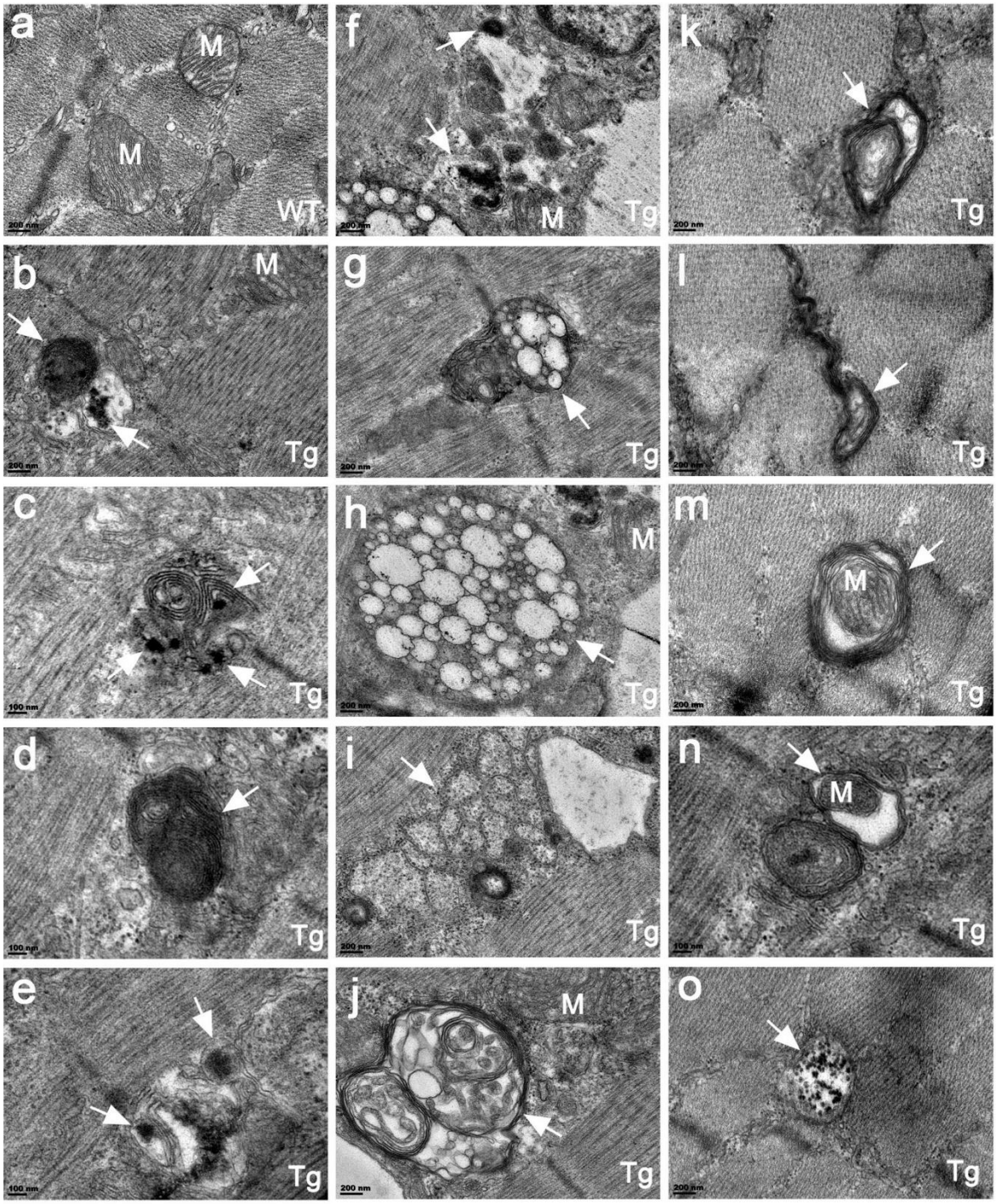

Extended Data Figure 8. **Transmission electron microscopy of quadriceps muscles from two-year-old wild-type (WT, panel a) and *ANT1^{Tg}*/+ (Tg, panels b-o) mice.** M, mitochondria; Arrows denote aggresome/lysosome-like structures that contain electron-dense aggregates (b-f), multivesicular vacuoles (g-j), multilamellar vesicles (k-l), mitophagic vesicles (m-n) and structures resembling glycophagy body (o).

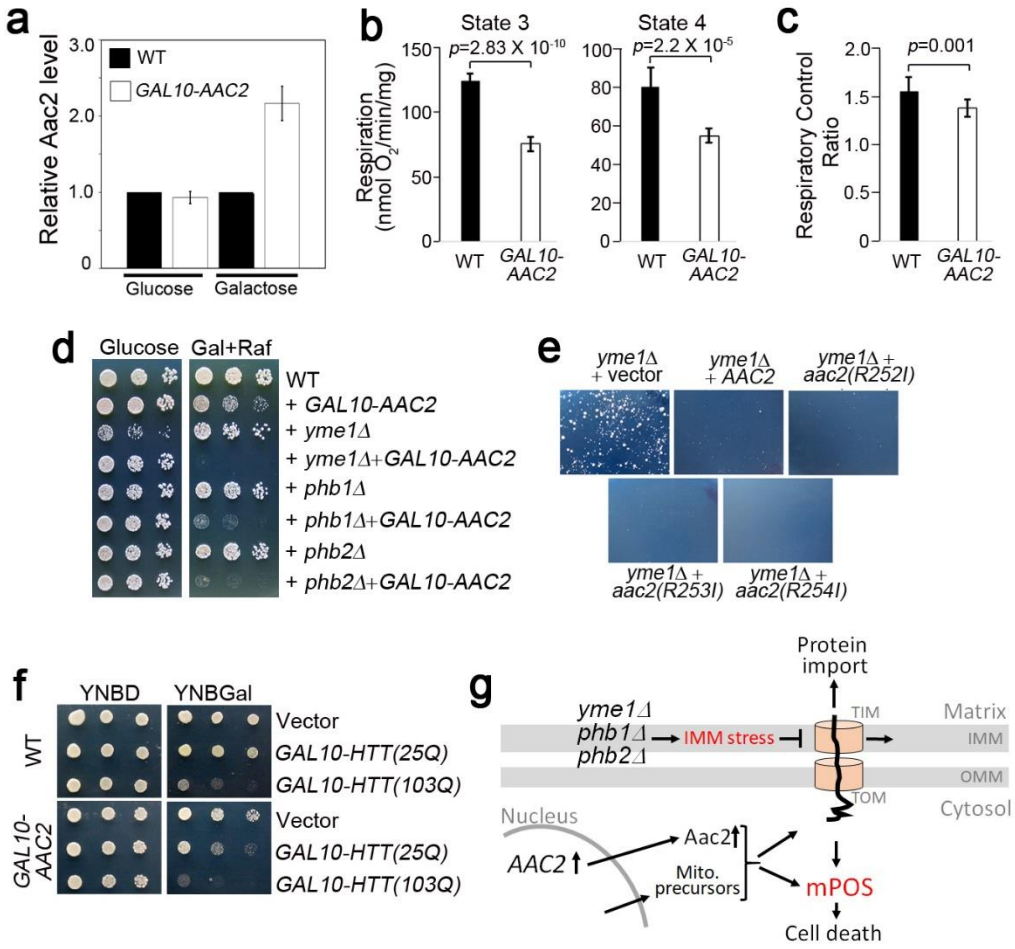

Extended Data Figure 9. **Moderate overexpression of the yeast *AAC2* gene, homologous to mammalian *ANT1*, is sufficient to induce mPOS.** (**a**) Relative Aac2 levels in yeast cells expressed from the galactose-inducible *GAL10* promoter. Cells were grown in complete medium containing 2% glucose or 2% galactose plus 2% raffinose before being lysed for western blot analysis. (**b**) and (**c**) Effect of *AAC2* overexpression on mitochondrial respiration and respiratory control ratio. (**d**) Overexpression of *AAC2* is synthetically lethal with the disruption of *YME1*, *PHB1* and *PHB2*, when cells were grown on the fermentable galactose (Gal) plus raffinose (Raf) medium. (**e**) Expression of *AAC2*, *aac2(R252I)*, *aac2(R253I*) and *aac2(R254I)* from the pRS425 (*LEU2*) vector inhibits the growth of *yme1Δ* cells. The *yme1Δ* mutant was transformed with the plasmids and selected for Leu^+ transformants on minimal glucose medium. Lack of viable transformants suggests synthetic lethality between *AAC2/aac2*-overexpression and *yme1Δ*. (**f**) Induction of *GAL10-AAC2* on minimal galactose medium renders cells hypersensitive to the expression of the aggregation-prone Htt(25Q) protein. Expression of Htt(103Q) alone is sufficient to inhibit cell growth without *AAC2* overexpression, which was used as a control. (**g**) Model predicting that Aac2 overloading induces mitochondrial Precursor Overaccumulation Stress (mPOS) in the cytosol, by saturating the cytosolic chaperone system and/or the protein import machinery. Error bars indicate standard deviations. *P* value was calculated by unpaired Student's *t* test.